Publisher's PDF, also known as Version of record

Link to published version (if available):
[10.1364/OE.25.026987](#)

Link to publication record in Explore Bristol Research
PDF-document

University of Bristol - Explore Bristol Research
General rights

Continuous-relief diffractive microlenses for laser beam focusing

MATTHEW DAY,[1,2,3] KAUSHAL CHOONEE,[1,*] DAVID COX,[1,4] MARK THOMPSON,[2] GRAHAM MARSHALL,[2] AND ALASTAIR G. SINCLAIR[1]

[1]*National Physical Laboratory, Teddington, TW11 0LW, UK*
[2]*Quantum Engineering Technology Labs, University of Bristol, BS8 1FD, UK*
[3]*Quantum Engineering Centre for Doctoral Training, University of Bristol, BS8 1FD, UK*
[4]*Advanced Technology Institute, University of Surrey, Guildford, GU2 7XH, UK*
[*]*kaushal.choonee@npl.co.uk*

Abstract: Microscale, continuous-profile, diffractive lenses have been fabricated and characterized. Lenses designed to operate at $\lambda_0 = 405$ nm were created by focused ion beam milling of a glass substrate. The micro-structured profile was analysed by confocal microscopy and optical performance was quantified by measurements of the transmitted laser beam profile. Lenses of size $125~\mu\text{m} \times 125~\mu\text{m}$, containing up to 18 annuli and focusing at $400~\mu\text{m}$, $450~\mu\text{m}$ and $500~\mu\text{m}$ have been made. Measured focused beams were in excellent agreement with the predicted performance. A maximum diffraction efficiency of 84 % and side-lobe suppression down to the 10^{-4} level can be achieved. The suitability of the lenses for interfacing with trapped-ion systems is outlined.

References and links

1. H. Haffner, C. F. Roos, and R. Blatt, "Quantum computing with trapped ions," Phys. Rep. **469**, 155–203 (2008).
2. R. Blatt and D. Wineland, "Entangled states of trapped atomic ions," Nature **453**, 1008–1015 (2008).
3. C. Monroe and J. Kim, "Scaling the ion trap quantum processor," Science **339**, 1164–1169 (2013).
4. S. Seidelin, J. Chiaverini, R. Reichle, J. Bollinger, D. Leibfried, J. Britton, J. Wesenberg, R. Blakestad, R. Epstein, D. Hume, W. Itano, J. Jost, C. Langer, R. Ozeri, N. Shiga, and D. Wineland, "Microfabricated surface-electrode ion trap for scalable quantum information processing," Phys. Rev. Lett. **96**, 253003 (2006).
5. G. Wilpers, P. See, P. Gill, and A. G. Sinclair, "A monolithic array of three-dimensional ion traps fabricated with conventional semiconductor technology." Nat. Nanotech. **7**, 572–576 (2012).
6. R. C. Sterling, H. Rattanasonti, S. Weidt, K. Lake, P. Srinivasan, S. C. Webster, M. Kraft, and W. K. Hensinger, "Fabrication and operation of a two-dimensional ion-trap lattice on a high-voltage microchip." Nat. Commun. **5**, 3637 (2014).
7. B. Tabakov, F. Benito, M. Blain, C. R. Clark, S. Clark, R. A. Haltli, P. Maunz, J. D. Sterk, C. Tigges, and D. Stick, "Assembling a ring-shaped crystal in a microfabricated surface ion trap," Phys. Rev. Appl. **4**, 031001 (2015).
8. N. D. Guise, S. D. Fallek, K. E. Stevens, K. R. Brown, C. Volin, A. W. Harter, J. M. Amini, R. E. Higashi, S. T. Lu, H. M. Chanhvongsak, T. A. Nguyen, M. S. Marcus, T. R. Ohnstein, and D. W. Youngner, "Ball-grid array architecture for microfabricated ion traps," J. Appl. Phys. **117**, 174901 (2015).
9. D. Kielpinski, C. Volin, E. W. Streed, F. Lenzini, and M. Lobino, "Integrated optics architecture for trapped-ion quantum information processing," Quantum Inf. Process. **15**, 5315–5338 (2016).
10. M. Ke, F. Zhou, X. Li, J. Wang, and M. Zhan, "Tailored-waveguide based photonic chip for manipulating an array of single neutral atoms," Opt. Express **24**, 9157 (2016).
11. C. C. Nshii, M. Vangeleyn, J. P. Cotter, P. F. Griffin, E. A. Hinds, C. N. Ironside, P. See, A. G. Sinclair, E. Riis, and A. S. Arnold, "A surface-patterned chip as a strong source of ultracold atoms for quantum technologies," Nat. Nanotech. **8**, 321–324 (2013).
12. M. Trupke, E. A. Hinds, S. Eriksson, E. A. Curtis, Z. Moktadir, E. Kukharenka, and M. Kraft, "Microfabricated high-finesse optical cavity with open access and small volume," Appl. Phys. Lett. **87**, 211106 (2005).
13. E. R. Dufresne and D. G. Grier, "Optical tweezer arrays and optical substrates created with diffractive optics," Rev. Sci. Instrum. **69**, 1974–1977 (1998).
14. H. Martinsson, J. Bengtsson, M. Ghisoni, and A. Larsson, "Monolithic integration of vertical-cavity surface-emitting laser and diffractive optical element for advanced beam shaping," IEEE Photon. Technol. Lett. **11**, 503–505 (1999).
15. V. Gandhi, J. Orava, H. Tuovinen, T. Saastamoinen, J. Laukkanen, S. Honkanen, and M. Hauta-Kasari, "Diffractive optical elements for optical identification," Appl. Opt. **54**, 1606 (2015).

16. H. Melkonyan, K. Al Qubaisi, K. Sloyan, A. Khilo, and M. S. Dahlem, "Gradient-index optical fiber lens for efficient fiber-to-chip coupling," Opt. Express **25**, 13035–13045 (2017).
17. E. W. Streed, B. G. Norton, A. Jechow, T. J. Weinhold, and D. Kielpinski, "Imaging of trapped ions with a microfabricated optic for quantum information processing." Physical review letters **106**, 010502 (2011).
18. A. Jechow, E. W. Streed, B. G. Norton, M. J. Petrasiunas, and D. Kielpinski, "Wavelength-scale imaging of trapped ions using a phase Fresnel lens." Opt. Lett. **36**, 1371–1373 (2011).
19. A. McDonald, G. McConnell, D. C. Cox, E. Riis, and P. F. Griffin, "3D mapping of intensity field about the focus of a micrometer-scale parabolic mirror." Opt. Express **23**, 2375–2382 (2015).
20. K. K. Mehta, C. D. Bruzewicz, R. McConnell, R. J. Ram, J. M. Sage, and J. Chiaverini, "Integrated optical addressing of an ion qubit," Nat. Nanotechol. **11**, 1066–1070 (2016).
21. H.-P. Herzig, *Micro-Optics: Elements, Systems And Applications* (Taylor & Francis, 1997).
22. B. C. Kress and P. Meyrueis, *Applied Digital Optics: From Micro-Optics to Nanophotonics* (Wiley, 2009).
23. A. Nottola, A. Gerardino, M. Gentili, E. Di Fabrizio, S. Cabrini, P. Melpignano, and G. Rotaris, "Fabrication of semi-continuous profile diffractive optical elements for beam shaping by electron beam lithography," Microelectron. Eng. **53**, 325–328 (2000).
24. W. Däschner, M. Larsson, and S. H. Lee, "Fabrication of monolithic diffractive optical elements by the use of e-beam direct write on an analog resist and a single chemically assisted ion-beam-etching step," Appl. Opt. **34**, 2534 (1995).
25. F. Schiappelli, R. Kumar, M. Prasciolu, D. Cojoc, S. Cabrini, M. De Vittorio, G. Visimberga, A. Gerardino, V. Degiorgio, and E. Di Fabrizio, "Efficient fiber-to-waveguide coupling by a lens on the end of the optical fiber fabricated by focused ion beam milling," Microelectron. Eng. **73**, 397–404 (2004).
26. I. Utke, S. Moshkalev, and P. Russel, *Nanofabrication using focused ion and electron beams: principles and applications* (Oxford University, 2012).
27. D. A. Pommet, M. G. Moharam, and E. B. Grann, "Limits of scalar diffraction theory for diffractive phase elements," J. Opt. Soc. Am. A **11**, 1827 (1994).
28. T. Shiono, T. Hamamoto, and K. Takahara, "High-efficiency blazed diffractive optical elements for the violet wavelength fabricated by electron-beam lithography," Appl. Opt. **41**, 2390 (2002).
29. M. A. Golub, "Generalized conversion from the phase function to the blazed surface-relief profile of diffractive optical elements," J. Opt. Soc. Am. A **16**, 1194 (1999).
30. G. Whyte and J. Courtial, "Experimental demonstration of holographic three-dimensional light shaping using a Gerchberg-Saxton algorithm," New J. Phys. **7**, 117 (2005).
31. Yongqi Fu, "Integration of microdiffractive lens with continuous relief with vertical-cavity surface-emitting lasers using focused ion beam direct milling," IEEE Photon. Techol. Lett. **13**, 424–426 (2001).
32. Y. Fu and N. K. A. Bryan, "Investigation of physical properties of quartz after focused ion beam bombardment," Appl. Phys. B **80**, 581–585 (2005).
33. S. Reyntjens and R. Puers, "A review of focused ion beam applications in microsystem technology," J. Micromech. Microeng. **11**, 287–300 (2001).
34. S. Juodkazis, L. Rosa, S. Bauerdick, L. Peto, R. El-Ganainy, and S. John, "Sculpturing of photonic crystals by ion beam lithography: towards complete photonic bandgap at visible wavelengths," Opt. Express **19**, 5802 (2011).
35. P. See, G. Wilpers, P. Gill, and A. G. Sinclair, "Fabrication of a monolithic array of three dimensional si-based ion traps," J. Microelectromech. Syst. **22**, 1180–1189 (2013).
36. M. Harlander, M. Brownnutt, W. Hänsel, and R. Blatt, "Trapped-ion probing of light-induced charging effects on dielectrics," New J. Phys. **12**, 93035 (2010).
37. A. M. Eltony, S. X. Wang, G. M. Akselrod, P. F. Herskind, and I. L. Chuang, "Transparent ion trap with integrated photodetector," Appl. Phys. Lett. **102**, 054106 (2013).
38. M. Ghadimi, V. Blūms, B. G. Norton, P. M. Fisher, S. C. Connell, J. M. Amini, C. Volin, H. Hayden, C.-S. Pai, D. Kielpinski *et al.*, "Scalable ion–photon quantum interface based on integrated diffractive mirrors," Quantum Inf. **3**, 4 (2017).
39. D. H. Slichter, V. B. Verma, D. Leibfried, R. P. Mirin, S. W. Nam, and D. J. Wineland, "UV-sensitive superconducting nanowire single photon detectors for integration in an ion trap," Opt. Express **25**, 8705–8720 (2017).
40. A. C. Fischer, F. Forsberg, M. Lapisa, S. J. Bleiker, G. Stemme, N. Roxhed, and F. Niklaus, "Integrating MEMS and ICs," Microsyst. Nanoeng. **1**, 15005 (2015).
41. G. D. Marshall, A. Politi, J. C. F. Matthews, P. Dekker, M. Ams, M. J. Withford, and J. L. O'Brien, "Laser written waveguide photonic quantum circuits," Opt. Express **17**, 12546 (2009).

1. Introduction

A wealth of research has been conducted into quantum information processing using trapped ions [1–3]. One of several challenges is to create systems that can be scaled to control a large number of ions. To date, much effort has been expended investigating different approaches to microfabricated, segmented, ion trap devices [4–8]; however the availability of suitable trap chips is only one part of the challenge. Bulk optical elements cannot be scaled to address

and image many individual particles stored at distinct locations in these devices [9]. This is similarly true for experiments with neutral atoms in chip-scale devices for quantum technology applications [10–12]. Micro-scale diffractive optical elements, previously used in numerous applications such as optical tweezer arrays [13], laser beam shaping [14], optical anti-counterfeit methods [15], and fiber-to-chip coupling [16], are a possible means to address this problem.

A few groups have investigated microfabricated diffractive elements for imaging the fluorescence from trapped ions [17, 18] as well as microfabricated mirrors for use in optical trapping of atoms [19]. For laser addressing of individual ions, grating couplers integrated to an ion microtrap device have also been demonstrated [20]. In these applications, lenses that exhibit high diffraction efficiency with minimal aberrations are desired. It is well known that for phase Fresnel lenses, discrete step profiles result in low diffraction efficiencies and so fall short of the performance prospects offered by continuous phase profiles [21, 22]. Grayscale electron-beam lithography [23, 24] and focused ion-beam (FIB) milling [25, 26] are methods capable of creating continuous profiles; both have the resolution required by the feature size in micro-lenses for visible and near infrared wavelengths. While the former is more efficient for writing larger arrays of elements over wider areas, the latter is better suited to rapid micromachining of prototypes. This is because micro-optical elements for atomic devices must be contained in ultra-high vacuum pressures of $\sim 10^{-11}$ mbar and this constrains the material to ones with low outgassing properties, such as optical glass. Glass can be structured by FIB milling in a single step process, whereas grayscale electron beam patterning requires both lithography and etching [24].

In this work we designed continuous-profile diffractive microlenses (DMLs) for focusing laser light at $\lambda_0 = 405$ nm. This wavelength is in the middle of the range 369 nm to 461 nm, which covers blue wavelengths needed for laser cooling and photoionization of Yb^+, Ca^+ and Sr^+. Six DMLs of dimensions 125 μm $\times$ 125 μm, containing up to 18 annuli, were machined into a glass substrate by FIB milling. Confocal microscopy was used to measure the fabricated surface profile and enable comparison to the designed surface. A laser at 405 nm and an imaging system were used to demonstrate the focusing properties of the lenses. Focusing distances, diffraction efficiencies and focused beam profiles were measured for all lenses.

2. Design

2.1. Background

DMLs were designed using scalar diffraction theory (SDT) as outlined in [21]. Applying the thin element approximation, DMLs implement a transfer function $T(x, y)$ such that the field after the DML plane is given by $E_2(x, y, 0) = T(x, y) \times E_1(x, y, 0)$, where $E_2(x, y, 0)$ and $E_1(x, y, 0)$ denote the fields after and before the lens respectively. $T(x, y) = e^{i\Psi(x,y)}$, where $\Psi(x, y)$ is the phase shift imparted by the DML. The optical field at any point (x', y', L) after the DML can be found by evaluating the diffraction integral:

$$E_2(x', y', L) = \frac{L}{i\lambda} \int \int_{-\infty}^{\infty} E_2(x, y, 0) \frac{e^{ikr}}{r^2} dx dy \,, \tag{1}$$

where $r = \sqrt{(x' - x)^2 + (y' - y)^2 + L^2}$. Assuming a normally incident beam, the phase shift is implemented as a height profile in a material of refractive index, n, as

$$h(x, y) = \frac{\lambda_0}{n - 1} \frac{\Psi(x, y)}{2\pi} \,. \tag{2}$$

The scalar approximation adopted in this work is favored for its simplicity. However, it is known to have limitations for dense and deep elements; these limitations have been studied numerically in [27], where the diffraction efficiency computed from SDT is compared against that obtained from a rigorous vector formulation that accounts for the thickness of the element. In the DMLs

considered here, the smallest relevant feature size illuminated by the laser beam is $\approx 8\lambda_0$ (see Section 2.4) and the deviation of SDT from an exact vector formulation is estimated to be $\leq 10\%$ according to [27]. This is considered to be acceptable for initial prototypes where imperfections in the fabrication (see Section 4.1) are likely to limit the performance. Diffractive elements can also exhibit polarization sensitivity and this is experimentally determined in [28]; here, the difference in diffraction efficiency between TE and TM incidence is estimated to be $< 1\%$ for gratings with feature sizes comparable to the DMLs in this work. Similarly, the expression for the height profile (Eq. (2)) assumes normal incidence. Although the incident beam is a diverging Gaussian beam in our arrangement (see Section 2.4) and the modified height expression for off-axis incidence as described in [29] should normally be considered, the difference in h is found to be at most 6 nm. This is less than the height error in the fabricated lenses (see Section 4.1) and the approximation of Eq. (2) is maintained.
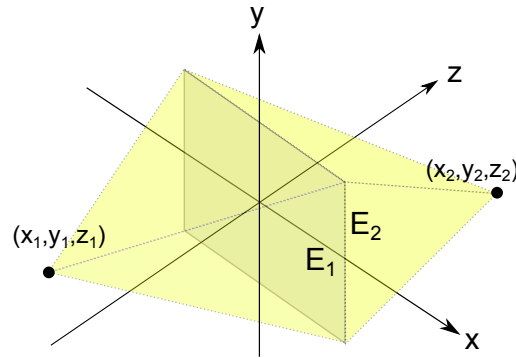
2.2. Phase transfer function for point sources

Fig. 1. The coordinate space used for designing DMLs using scalar diffraction theory. A point source at (x_1, y_1, z_1) is mapped onto a point image at (x_2, y_2, z_2) by the DML at the $z = 0$ plane.

The phase shift required to map a point object to its image can be derived by considering the optical path lengths of the relevant rays, as illustrated in Fig. 1. Assuming a lossless, homogeneous, and isotropic media, the phase shift, $\Psi_{PS}(x, y)$ is given by

$$\Psi_{PS}(x, y) = \frac{2\pi}{\lambda_0}\left(-n_2\sqrt{(x - x_2)^2 + (y - y_2)^2 + z_2^2} - n_1\sqrt{(x - x_1)^2 + (y - y_1)^2 + z_1^2} \right) \quad (3)$$

where n_1 (n_2) is the refractive index of the medium before (after) the DML. The required DML height profile is obtained by wrapping $\Psi_{PS}(x, y)$ to $[0, 2\pi)$ and replacing in Eq. (2).

2.3. Phase transfer function for finite sources

In practice, the object and its image (both assumed to be Gaussian beam waists) are finite and, while $\Psi_{PS}(x, y)$ provides a starting value, a modified phase function, $\Psi_G(x, y)$, is required to ensure accurate focusing. To obtain a lens focusing at $(0, 0, z_D)$, the field intensity at that point must be maximized. This is done iteratively; for a given Gaussian waist at (x_1, y_1, z_1), $E_1(x, y, 0)$ is determined, the design parameter z_2 is adjusted, $|E_2(0, 0, z_D)|^2$ is evaluated using Eq. (1) and this is repeated until a maximum has been found. With this value of z_2, a modified phase profile, $\Psi_G(x, y)$, can be obtained.

Phase profiles were generated for focusing a Gaussian input beam in glass ($n_1 = 1.53$) with beam radius $w_0 = 3.75$ μm at $(x_1, y_1, z_1) = (0, 0, -1000)$ μm and focusing at 500 μm, 450 μm and 400 μm in air ($n_2 = 1$). The corresponding values of z_2 are 521 μm, 466 μm and 412 μm.

Other techniques such as the Gerchberg-Saxton procedure [30] would allow arbitrary field shaping, however the single-parameter optimization method is effective and currently sufficient for DML design. We also note that for axial designs with $x = y = 0$, Gaussian beam propagation equations can be combined with the lens maker's equation to derive an approximate expression for z_2. This approach yields values of z_2 within 2 μm of our numerical method.

The advantage of the optimization approach is that it can be used to design lenses for focusing off-axis ($x_D, y_D \neq 0$). However, we found that even with modest angles ($\lesssim 10°$), the minimum lens annulus width approaches 1 μm with aspect ratio (defined as the height to annulus width) of ≈ 0.8. As will be discussed in Section 4, high aspect ratio structures are difficult to realize in practice and this ultimately limits the lens performance. Moreover, the error in the SDT formulation increases with off-axis operation; for example, for feature sizes of $10\lambda_0$, the errors become $\leq 15\%$ and $\leq 20\%$ for incidence angles of $20°$ and $30°$ respectively [27]. Should the fabrication limitations be overcome in future work, a rigorous vectorial formulation will be required.
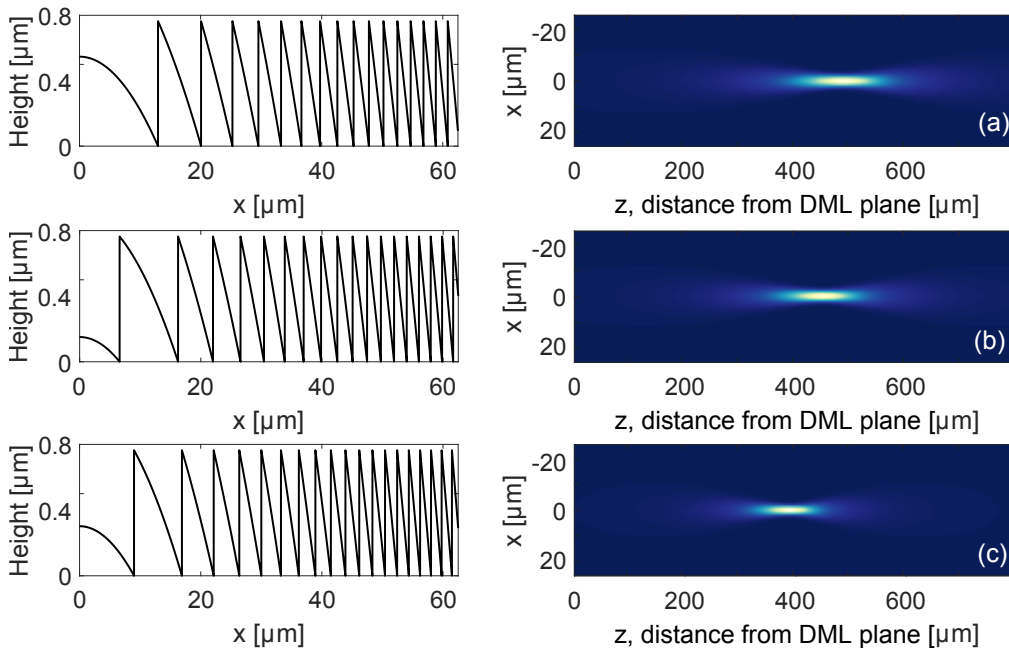

Fig. 2. Simulations of the output field of DMLs at $y = 0$ for a Gaussian source of $w_0 = 3.75$ μm at a wavelength of $\lambda_0 = 405$ nm. The corresponding radially symmetric height profile in BK7 glass is displayed to the left of each simulation. The DMLs have been designed to focus at (a) 500 μm, (b) 450 μm, and (c) 400 μm from the lens plane. These are referred to as lens designs A, B and C respectively throughout this report.

2.4. Simulations

The performance of the DML inducing a phase shift of $\Psi_G(x, y)$ was confirmed by numerically evaluating Eq. (1) to find the field distribution. Examples of designed lenses and their simulation results are shown in Fig. 2. By replacing the input source by a collimated beam and evaluating Eq. (1), the focal length f can be estimated, and these are 290 μm, 272 μm, and 253 μm for lens

design A, B and C respectively. The NAs can be found as $n_2 \sin[\arctan(D/2f)]$, where D is the lens diameter. With the current optical arrangement described, the waist of the beam impinging on the DML is $w(z = 0) = 22.8$ μm. Therefore, 99.9% of the power of the incident Gaussian beam is contained within a radius of $2w(z = 0) = 45.6$ μm (i.e. within a diameter of $4w$) of the center of the lens and only this region of the lens is in practice illuminated. Hence, $D = 91.2$ μm and the NAs are 0.16, 0.17 and 0.18 for designs A, B and C. The partial illumination also implies that the minimum lens annulus width seen by the beam is ≈ 3 μm (or $\approx 8\lambda_0$), which corresponds to a maximum aspect ratio (defined as the height to annulus width) of < 0.3.

3. Methods

3.1. FIB machining of DMLs

The proposed DML designs were fabricated on BK7 glass substrates (25 mm diameter, 5 mm thick) by FIB machining in a process similar to [23, 31]. Briefly, a focused beam of Ga^+ ions with a beam current of 3 nA and accelerating voltage of 30 kV, corresponding to a spot size of ~ 90 nm (FWHM) was raster scanned over a target area to etch the substrate to a precise shape (FEI Nova NanoLab 600). The physical profiles were discretized to 0.1 μm/pixel laterally, while the height was defined by 1150 steps. In each etch step, up to ~ 0.65 nm was etched. The fine steps, combined with the finite ion beam spot, yield a continuous profile. Initially, calibration of the FIB process was approximated using Si substrates, which we found to etch at a similar rate as glass. It was more practical to observe Si substrates *in-situ* with a scanning electron microscope (SEM); an image of such a test structure is shown in Fig. 3(a), highlighting the continuous features. Glass lenses were then milled using the same recipe, with a minor correction to account for a small difference in sputter yield between Si and glass. The lens profiles were measured using a scanning laser confocal microscope (Lext OLS 4000, Olympus Corporation) and the milling dosage was fine-tuned until the desired profile was obtained. The glass substrates were coated with a thin (~ 50 nm) layer of Al prior to milling so as to avoid artifacts due to charge buildup; the metal in the lens area was removed by the impinging beam but empirically, we find that the fabrication process was not affected despite the area of the lens. Fig. 3(b) shows an SEM image of a typical BK7 glass substrate containing several lenses as well as alignment and test structures.

3.2. Experimental arrangement

The optical apparatus used to characterize the fabricated lenses is illustrated in Fig. 4. It consists of three parts: (i) the mode preparation optics, (ii) the DML under test, and (iii) the imaging system. The input beam for DML testing (assumed to be a good approximation to Gaussian) was prepared by directing light from a 405 nm laser diode into a single-mode fiber, collimating to free-space and focusing using a 10× microscope objective. The latter is mounted on a translation stage (with a resolution of 10 μm) such that the beam waist at the output of the objective can be positioned accurately with respect to the DML plane. The DMLs under test were mounted on appropriate stages having translational (x, y, z) and rotational (the xy-plane) degrees of freedom. The DML plane is defined as the $z = 0$ reference plane. After the DML, the propagating beam was imaged using an Olympus MPLFLN 100× objective placed 16.2(1) cm from a CCD designed for beam profiling (DataRay Inc., WinCamD UCD12). This assembly, referred to as the beam profiler, is mounted on a motorized linear stage with a repeatability of ±1 μm (Newport Corp., LTA-HL). At this objective-to-CCD distance, the magnification at the CCD plane was measured to be 89.0(5) using a calibration graticule. Together with the CCD pixel size of 4.65 μm, this provides adequate resolution in the image plane (assuming no significant aberrations from the infinity-corrected objective lens). The extent of the object plane being imaged corresponds to 72.1 μm × 54.3 μm.

Spatial initialization was performed by imaging the DML surface directly with the beam

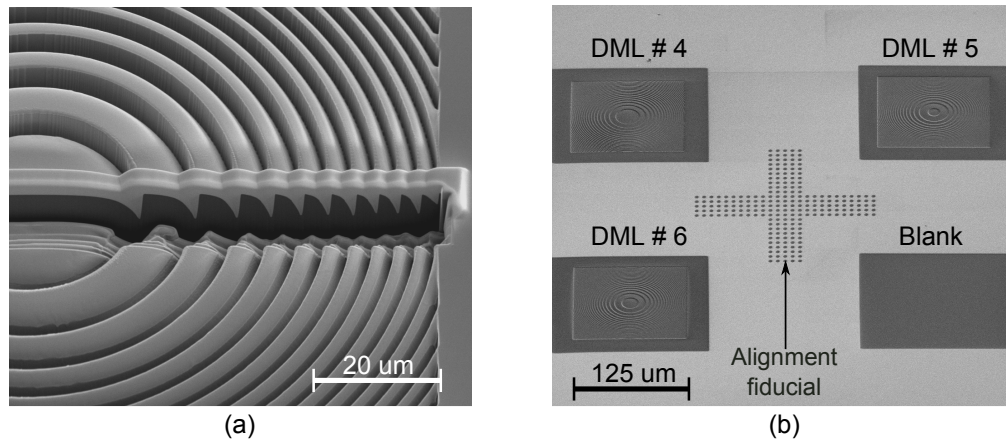(a)   (b)

Fig. 3. (a) SEM image of a Si sample used to test the milling pattern geometry. The sample was prepared by milling a complete lens, then a narrow ($\sim 5~\mu$m) strip of Pt was deposited across the lens using FIB-induced deposition, and finally a trench was milled through a section of Pt on Si to reveal the profile of the lens. (b) SEM of a BK7 glass substrate carrying DML 4, 5, and 6 as well as a blank opening. Light areas indicate metal-coated and dark areas are BK7 glass.
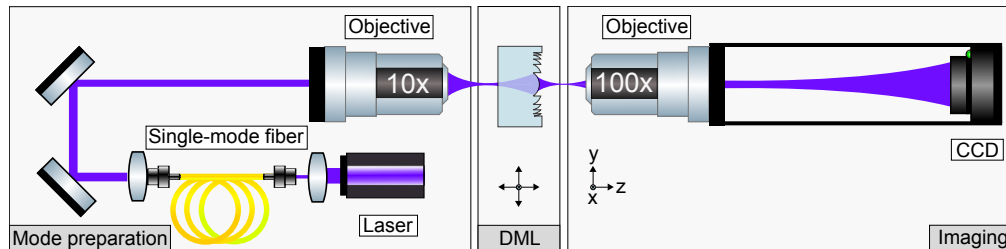

Fig. 4. DML characterization set up. Mode preparation consisted of coupling a 405 nm laser diode into single mode fiber before collimating and centering on a 10x objective to focus light to beam radius $w_0 = 3.75~\mu$m at $z = -1000~\mu$m from the DML chip surface. The source beam then expands to a radius of $w(z = 0) = 22.8~\mu$m at the surface of the DML, where it is focused. Note that 99.9% of the incident beam overlapped with a central area of the DML of radius $2 \times 22.8~\mu$m. The focused spot created by the DML was imaged onto a CCD sensor via a 100× imaging objective.

profiler allowing $z = 0$ to be determined to within $\pm 1~\mu$m. The DML substrate was then translated in the xy-plane so that the incident beam passed through the blank window (see Fig. 3(b)). The source beam objective was adjusted in the z-direction until the beam radius at the DML plane $w(z = 0) = 22.8~\mu$m. This arrangement corresponds to a Gaussian source with $w_0 = w(z = -1000~\mu\text{m}) = 3.75~\mu$m, as per the design in Section 2. The substrate was finally translated laterally to the position of the element to be tested.

The transmitted field after the DMLs was mapped by acquiring beam profiles at 1 μm intervals from $z = 0~\mu$m to $z = 800~\mu$m. At the focal plane of each DML, additional images with different exposures were acquired and merged to form a composite beam profile overcoming the dynamic range (100 : 1) of the CCD [20]. A detailed calibration of the background-corrected CCD response was made for each exposure time used, thus ensuring the accuracy of processed data across the full range. Typically, images at 5 different exposure durations were recorded, thus enabling the beam intensity to be recorded over 5 orders of magnitude.

A key parameter for DML characterization is the diffraction efficiency, η_D, defined as the ratio of power in the desired order to the total power transmitted [21, 22]. This was determined by measuring the beam profile at $z = 0$ μm (which is not diffracted and represents the total power) and that at the focal plane of the DML. The power was calculated by integrating the intensity profiles measured on the CCD with the integration limits restricted to a radius $r = 2w(z)$. We further quantify the quality of the beam by extracting the side-lobe intensities at $x = \pm 2w_0$ and $x = \pm 4w_0$ from the composite, high dynamic range, beam profiles at the focal plane.

4. Results

4.1. Fabrication

DMLs were fabricated using the method described in Section 3.1. Using lens design A as a template, a suitable FIB milling recipe was developed over several iterations. Each time, the height profile and the diffraction efficiencies were measured and used to refine the process. We observed empirically that over-etched structures performed worse than under-etched ones and therefore applied a conservative milling dose. After optimization, two substrates were patterned. The first comprised DML 1, 2 and 3 which were all with design A, whilst the second contained DML 4, 5 and 6 corresponding to designs A, B and C respectively. The FIB recipe developed for lens design A was adopted for lens designs B and C. Fig. 5 shows the height profiles measured by confocal microscopy (at $y = 0$) of DML 2 and 5, with their designs overlaid for comparison.

Due to an initial oversight in the model, the phase profiles $\Psi_G(x, y)$ used to fabricate the lenses are slightly different to those presented in Section 2. This difference results in a shift in the lateral positions of the crests which increases with the radius. For example at lens positions $x \le 20$ μm, the profiles are indistinguishable; at $x = w = 22.8$ μm and $x = 2w = 45.6$ μm, the lateral shifts are < 100 nm and < 360 nm respectively. Numerical simulations confirm that the associated change in optical response is negligible in comparison to the measured difference between experiment and simulation (see Section 4.2). This oversight has no significant influence on the results and conclusions of this work; in the remainder of this manuscript, the fabricated lenses are compared to their as-designed height profiles (Fig. 5). Similarly, the as-designed phase profiles are used in numerical simulations that are compared to measured performance (Fig. 6, 7, 8).

The profile of the fabricated lens deviates from the design in the following ways. Firstly, the structures are not milled to completion, with the result that the low-relief features (i.e. troughs) are underetched. In DML 5 (Fig. 5(b)), the central annulus has a significant fractional error as it is low relief by design, unlike DML 2. Separate to the systematic underetch, the depths of the troughs become shallower further from the center while the crests get more rounded. The flattening of the trough is attributed to re-deposition and accumulation of material at the bottom of the tight trench following beam-induced sputter etching [26]. Rounding of the crest is attributed to the finite volume of the focused ion beam, whereby additional material is removed by the beam wings. The extent of both effects increases with the aspect ratio of the annulus.

In future fabrication iterations these artifacts could be minimized; the etch dose could be further adjusted for each lens type until the structure is milled to sufficient depth, while the crest rounding could be reduced by using a smaller beam diameter beyond a certain depth to avoid collateral damage. However, it is unlikely that both artifacts can be optimized simultaneously and the structure aspect ratio appears to be the limiting factor; this can already be observed in the outermost annuli of DML 5 (Fig. 5 (b)).

Lastly, we note that a side effect of Ga$^+$ FIB is ion implantation. This effect was not investigated in this work, however, others have reported blue shifting of the lasing wavelength in GaN lasers [26], a ~ 10 % drop in transmission and an increase in refractive index ($\Delta n \sim 0.5$) at 400 nm in quartz [32], or 30 nm thick Ga enrichment in silicon with modified chemical properties [33]. We can estimate the effect of Ga implantation in BK7 by assuming a similar
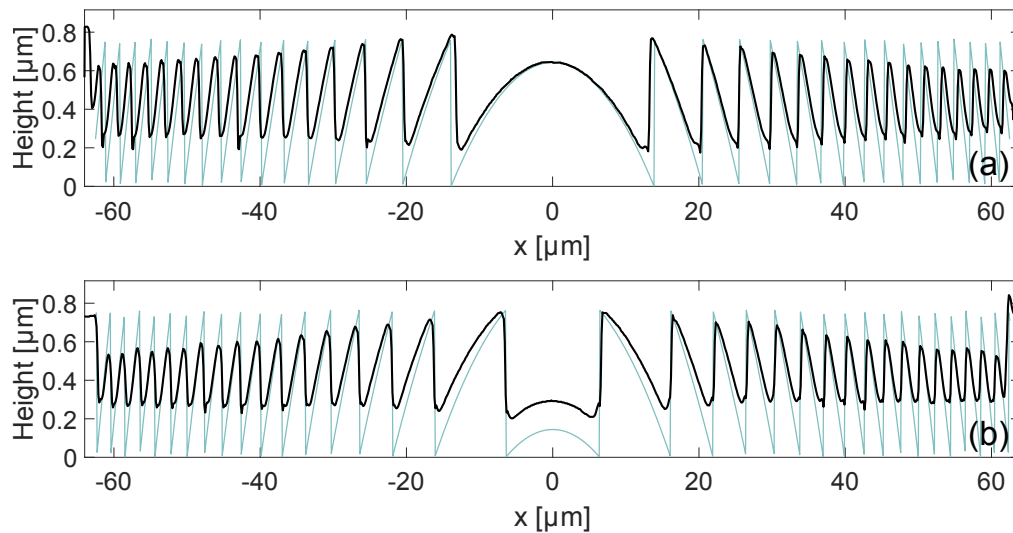
Fig. 5. Measured profiles (dark) of typical fabricated DMLs and design profiles (light) for comparison (a) DML 2, and (b) DML 5.

implantation depth as Si and the same Δn as quartz. The change in optical path is then ~ 15 nm, which amounts to ~ 2 % of the DML height and therefore the effect on the phase transfer function will not be significant.

4.2. Optical characterization

The fabricated lenses were characterized optically and their performance is summarized in Table 1. The first substrate, carrying DMLs 1, 2 and 3 with design A (focusing at $z = 500$ μm) demonstrates the repeatability of the process, with all three lenses focusing to within ~ 1 % of their designed value, achieving $\eta_D > 80$ % and relative side-lobe intensities of 10^{-4} at $x = \pm 4w_0$. Beam propagation along the z-axis is illustrated in Fig. 6; part (a) shows the optical intensity variation in the xz-plane for DML 2, while part (b) compares the measured beam intensity on the optical axis ($x = y = 0$) with the values expected from the simulation of the designed lens. The measured beams exhibit a shorter depth of focus and a very weak local maximum at $z \approx 175$ μm due to the second diffractive order (the focal length f is now $f/2$, and the image point is ≈ 186 μm, which is close to the observed peak position); these deviations are attributed to the imperfect profile of the fabricated lens. At the focal plane, the beam quality was examined in more detail through high dynamic range images as described in Section 3.2. Data for DML 2 is shown in Fig. 7; part (a) shows a color map of the focused beam over a 40 μm × 40 μm area, while part (b) shows the beam intensity at $y = 0$ μm with the simulated beam profiles from the designed and fabricated lens, and a Gaussian fit overlaid for comparison. The deviation in the measured beam waist ($w_0 = 3$ μm) from the design is ~ 5 % while the relative optical intensities away from the beam center are $\sim 10^{-4}$, corresponding to that expected from a simulation using the as-fabricated lens profile. DMLs 1 and 3 exhibit similar beam profiles.

In the second substrate, three lenses with designs A, B and C were patterned to demonstrate alternative focal lengths. The results are presented in Fig. 8, where the measured beam intensity along the z−axis is compared to simulations of the ideal lenses, along with a composite image of the beam at focus. The measured distances of the beam waist from each lens, summarized in Table 1, agree with designed values to within 2.5 %. In terms of diffraction efficiencies η_D, DML 4 is comparable to DML $1 - 3$ as expected, while DML 5 and 6 are significantly lower. This is

Table 1. Summary of measured optical performance of fabricated DMLs. All fabricated lenses focus within 10 μm of their design length, while only DML $1-4$, of design A, achieve high diffraction efficiencies of > 80 %

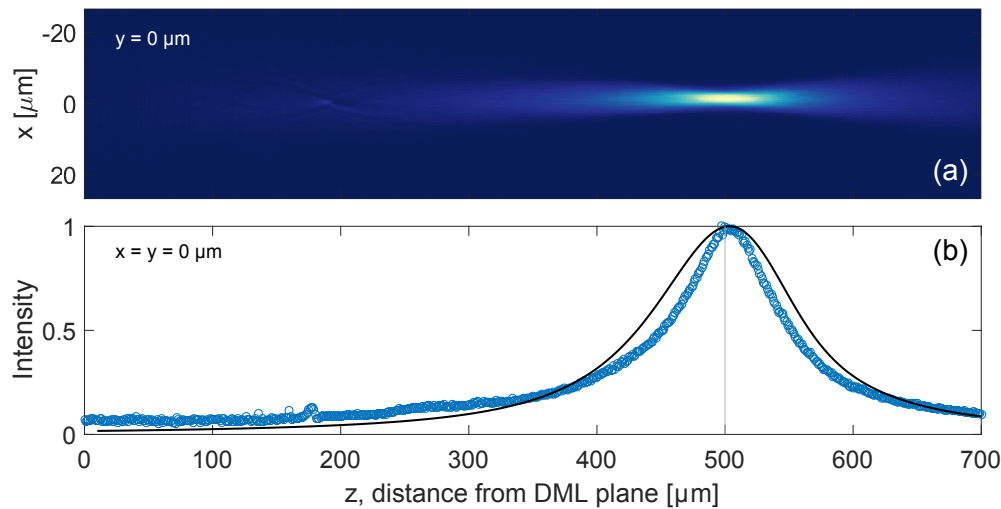| DML	Waist distance from lens, z_D (μm)		η_D (%)	Relative intensity	
	Design	Measured		$x = 2w_0$	$x = 4w_0$
1	500	505	80.9	1×10^{-2}	2×10^{-4}
2	500	503	84.0	7×10^{-3}	3×10^{-4}
3	500	498	82.4	2×10^{-2}	5×10^{-4}
4	500	507	77.2	1×10^{-2}	3×10^{-4}
5	450	445	53.6	5×10^{-3}	7×10^{-4}
6	400	390	50.7	8×10^{-3}	2×10^{-4}

Fig. 6. Measured propagation of lens 2, designed to focus at 500μm. (a) Color map of the measured beam profile after the DML plane. Dark represents an intensity of 0, and bright represents a normalized intensity of 1. (b) The measured intensity (open circles) along the optical axis, z, with equivalent simulation of the design profile for comparison (solid line).

due to an under-etched central dome (see Fig. 5(b)) which overlaps with ≈ 25 % of the incident beam power and strongly influences the optical transfer function. High dynamic range beam profiles at the focus position of DML 5 are shown in Fig. 7(c, d). The spot at the focal plane is still efficiently shaped with background intensities of $\sim 10^{-3}$ relative to the peak. However, the low value of $\eta_D = 53.6$ % implies that significant power appears outside the field of view of the beam profiler.

5. Discussion

An important performance measure for DMLs is diffraction efficiency; in this work we achieved $\eta_D = 84$ %. An exact comparison with other work is not straightforward and η_D is often application dependent [22]. Our best measured result equals the highest reported efficiency for DMLs in glass (65 μm diameter) [32]; however, in that work measurements of lens topology and beam quality were not presented. In our work, η_D was limited by the phase contrast due to fabrication imperfections, which is affected by two factors: 1) the under-etched lens depth at the
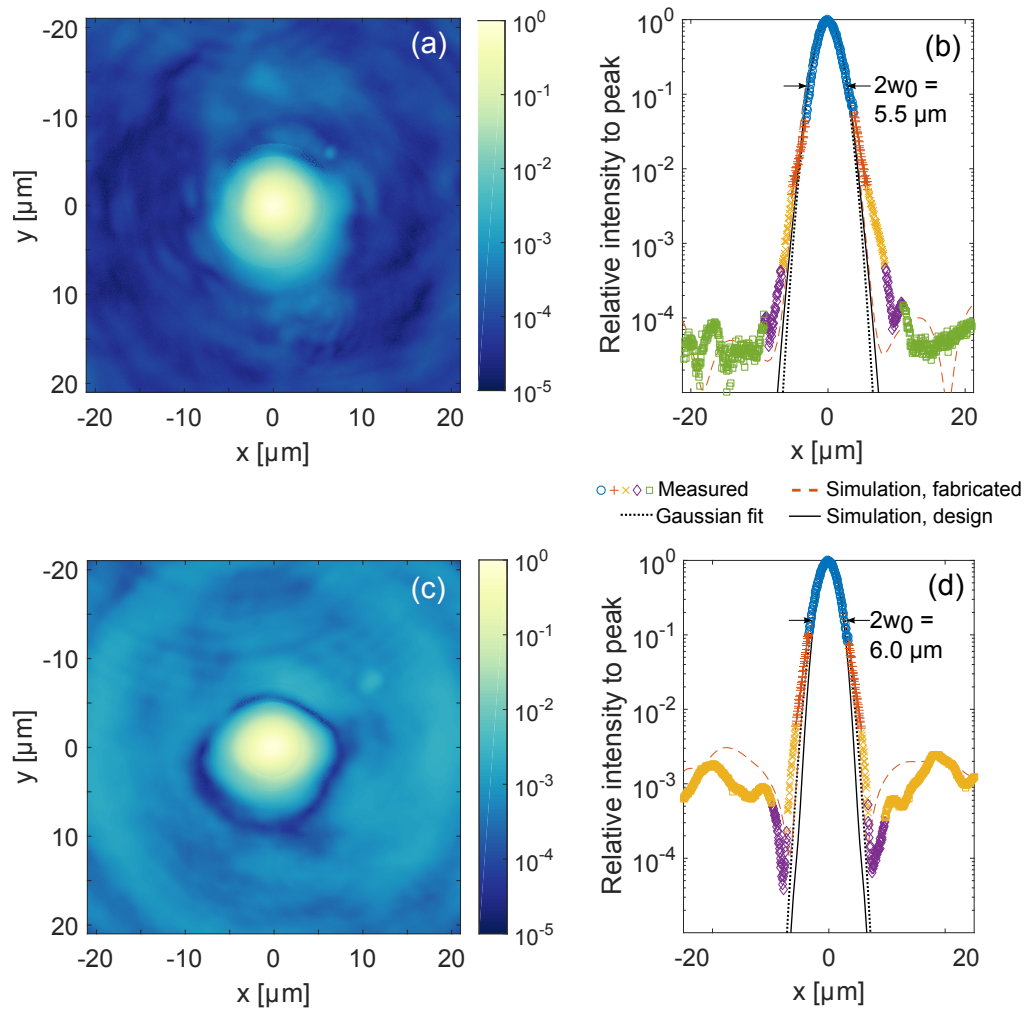
Fig. 7. Beam profile at 500 μm from the plane of DML 2 (design A): (a) 2D profile normalized to the peak intensity, (b) 1D log plot along the x-axis of the beam profile at $y = 0$ demonstrating the background intensity away from the peak and deviation from simulations of the designed and fabricated lens. (c) and (d) are corresponding plots for DML 5 (design B). In (b) and (d), the data acquired with different exposure times are represented by different colors and symbols. In (b) these are 0.2 ms (blue), 0.8 ms (orange), 6.8 ms (yellow), 64.9 ms (purple) and 118.4 ms (green). In (d) these are 0.2 ms (blue), 1.1 ms (orange), 10.3 ms (yellow), and 101.3 ms (purple).

central dome, and 2) the increasing aspect ratio at the outermost annuli. For the same lens transfer function, the aspect ratio can be reduced by using media of higher refractive index, which requires a shallower etch depth (Eq. (2)). An example of this approach is the DML reported in [31] where $\eta_D = 90$ % was obtained in a GaAs substrate at $\lambda = 980$ nm ($n \approx 3.5$, 140 μm diameter, 8 annuli, NA = 0.29). For visible wavelengths, TiO$_2$ ($n \approx 2.5$) is a possible option, requiring a depth of only 270 nm at $\lambda_0 = 405$ nm (cf 760 nm on glass). Forming TiO$_2$ photonic components by FIB machining has been demonstrated [34], however the moderate transmittance of this material in the visible could be a limitation. Alternative materials could include, e.g., sapphire, AlGaN or GaN. Furthermore, using high refractive index substrates aids application of the DML to a wider
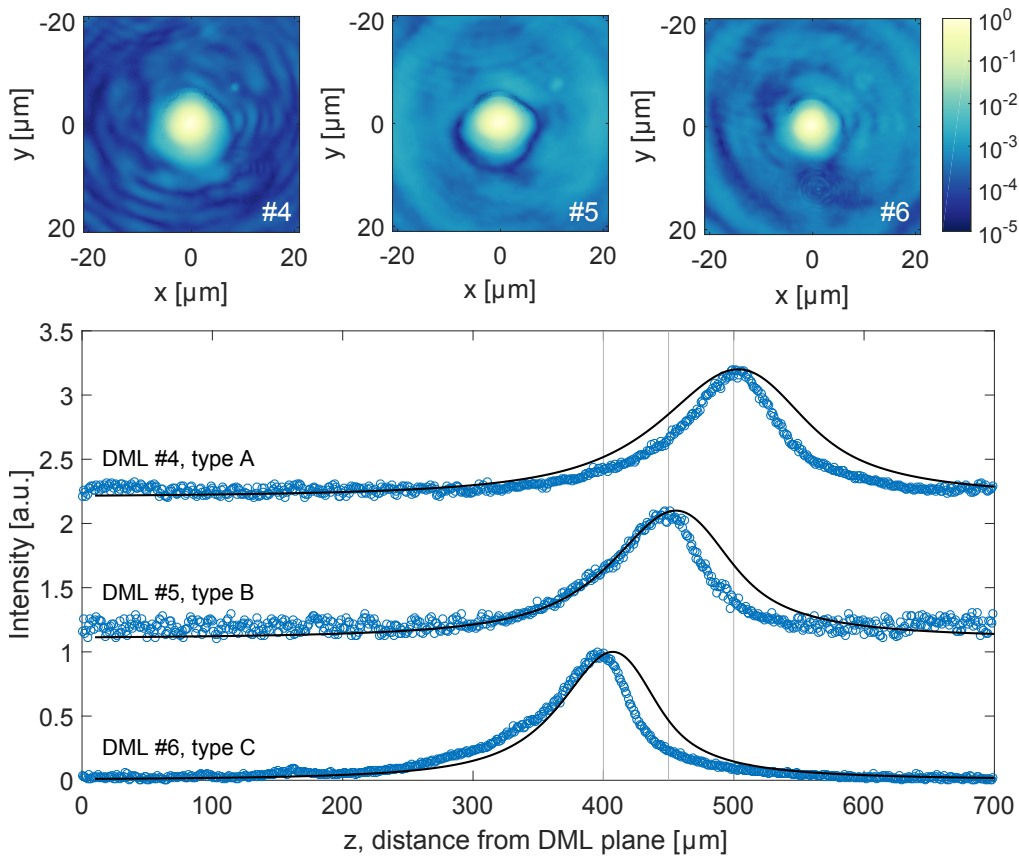
Fig. 8. Intensity propagation of lenses 4, 5 and 6 along the optical axis. The measured optical intensity (open circles) at $x = y = 0$ is shown along with the equivalent simulated profile from the design (solid line). The data for different lenses has been offset for clarity.

range of wavelengths (blue to NIR), since the lens thickness h scales as $\lambda/(n-1)$ while the aspect ratio is estimated to increase slowly as $\lambda^{1/2}$. This extended wavelength range is important for DMLs to be used in the focusing of lasers beams onto atomic particles such as Sr^+ and Ca^+.

In trapped-ion quantum gates, maximizing the fidelity of state detection and coherent control routines is important. To achieve this, it is a prerequisite that the laser beams focused on the ion(s) have the majority of the optical power confined to the focused spot, with side-lobes strongly suppressed. This is important for beams that perform cooling and state detection, as well as those that coherently manipulate the quantum states. In the former, scattered light decreases the state detection fidelity though an increased background and hence decreased signal-to-noise. In the latter, optical power in side-lobes can result in crosstalk errors when addressing individual ions in a string (where the error scales as the relative intensity [20]). In earlier work [20], a binary grating coupler operating at $\lambda = 674$ nm was used to address a Sr^+ ion. In that work the relative side-lobe intensities were measured to be 10^{-2} and 10^{-3}, at distances of $x = 2w_0$ and $x = 3.75w_0$ from the beam center, respectively. Applying the same criterion to the DMLs in our work, we find that we can achieve corresponding intensities down to 10^{-3} and 10^{-4}, which are a factor of 10 better than those of [20]. By optimizing the fabrication process to achieve the correct etch depth in the continuous profile, side-lobe intensities could be suppressed further.

Our demonstrations concentrated on focusing distances of 500 μm, with application to ion microtraps of a 3D electrode geometry [5, 35] in mind. It is advantageous to position optical

elements far from the ion to avoid distortion of the trapping potential due to charge accumulation on dielectrics [36]. DMLs 4-6 show that variations in focusing distance z_D can be achieved, with 400 μm being the lower limit of this work. Shorter z_D for the same input beam parameters requires lenses with higher aspect ratios (see Fig. 2). On the other hand, lenses with longer z_D require larger annuli widths, so become easier to fabricate, and this offers the prospect of micro-lenses at a greater distance from the trapped ion. If required, a thin transparent, conducting coating on the dielectric could suppress electrostatic charging [37].

Integration of optical elements of the form demonstrated here with ion microtrap chips remains a key challenge. Other groups have explored monolithic integration of optical elements with RF trap chips; focusing couplers [20], diffractive mirrors [38] and photodetectors [39] have been demonstrated. Such structures have the advantage of alignment accuracy at the resolution of the lithographic process. However, optimizing the requirements of the trapping potential (i.e. electrical) and for ion addressing (i.e. optical) may require compromises in the choice of material system. In a different approach, we propose to create separate microtrap and photonic chips using substrates and processes optimized for each, which are then bonded to form a hybrid microstructure. Such an approach is commonly used in MEMS and ICs, where sub-micrometer alignment accuracy is possible [40]. Looking towards such a photonic chip, we are currently investigating DMLs at the end of laser-written waveguides in glass [41].

6. Conclusions

Continuous relief DMLs have been fabricated using FIB milling in BK7 glass substrates. Repeatability of the fabrication process and an ability to fabricate DMLs with different focal lengths have been demonstrated. With a lens focusing at a distance of 500 μm, we achieved a diffraction efficiency of 84 % into spot size of $2w_0 = 5.5$ μm, with side-lobe intensities suppressed to the 10^{-4} level. The fabrication technique is therefore suitable for prototyping photonic components such as imaging and focusing elements for trapped-ion systems, as well as a range of other applications. Furthermore, the designs explored in this work could be realized using a grayscale electron beam process combining lithography and parallel etching [24]; this is more suitable for optical platforms containing large arrays of lenses.